EXPERIMENT ON STABLE AND UNSTABLE FLUTE
OSCILLATIONS IN A SCALED DOWN MIRROR MACHINE

by

T. Y. Chang

ELECTRONICS RESEARCH LABORATORY

College of Engineering
University of California, Berkeley
94720

ABSTRACT

The behavior of flute modes in a mirror machine was studied in a scaled experiment using a potassium plasma generated by surface emission from a centrally located ionizer-cathode. The scaling concept and its general application are discussed. Preliminary results of the experiment are also presented. It is found that the plasma is quite reproducible and can be partially expanded away from the ionizer-cathode by magnetic decompression. Various flute oscillations were observed and their mode numbers and phase velocities carefully determined. Further improvements in the measurement of both the electric field and the flute growth (or transport) rate are necessary.

TABLE OF CONTENTS

INTRODUCTION

An experimental study of the flute instability using a scaled mirror machine was proposed earlier by Birdsall, Byers and Chang [1], following a suggestion by C. W. Hartman. A device was subsequently built and the experimental work is still in progress. This interim report summarizes the results of research as of March 1967.

The concept of scaling a plasma for the study of flute oscillations is explained in Sec. 1. The experimental device and the magnetic decompression scheme for separating the plasma from the ionizer-cathode are described in Sec. 2. The experimental results are discussed in Sec. 3.

1. SCALING CONCEPT

This experiment utilizes a low density (10^8 - 10^9 cm^{-3}) potassium plasma in a kilogauss range magnetic field for studying the flute instability caused by the magnetic field curvature. An important feature of this experiment is its correspondence with the case of a denser, high-temperature plasma confined in a much stronger magnetic field. The correspondence is a consequence of the law of similitude for flute modes ($k_{11} = 0$, $\nabla \times \overline{E} = 0$, $\omega \ll \omega_{ci}$), which can be stated as follows: [1], [2].

As far as flutes are concerned (even in the nonlinear limit), two geometrically similar plasma systems are equivalent provided that the distribution functions satisfy the following relation,

$$\frac{m_a f_a(\overline{r} L_a^{-1}, \overline{v} L_a^{-1} \omega_{cia}^{-1})}{\epsilon_0 B_a^2(\overline{r} L_a^{-1})} = \frac{m_b f_b(\overline{r} L_b^{-1}, \overline{v} L_b^{-1} \omega_{cib}^{-1})}{\epsilon_0 B_b^2(\overline{r} L_b^{-1})},$$

where L_a and L_b are the characteristic lengths for

systems "a" and "b".

By the word "equivalent" we mean that for each normal mode

$\phi_a(\overline{r} L_a^{-1}, \omega_{cia} t)$ in system "a", there is a corresponding normal mode

in system "b" given by $\phi_b = \phi_a(\overline{r} L_b^{-1}, \omega_{cib} t)$. The following paragraph

offers in less exact terms some further explanations of this law of

similitude.

If the magnetic field B, the density n, the temperature T,

and the size L of a plasma system are varied in such a way that the

relative magnitudes of the radius of curvature, the mirror-to-mirror

distance, the wall radius, the ion gyroradius, and the ion Debye length

remain unchanged, then the solutions for flute modes are unaltered

except for an obvious change in length scale and a possible change in

time scale. If the scaling of the system involves a change of ω_{ci}, then

the resulting frequencies of oscillations are also changed by the same

factor as ω_{ci}.

Scaling relations among different plasmas can be determined

quickly with the help of Fig. 1. For instance, the speed of a 0.1 eV, K^+

ion can be found in the lower left section of the figure to be approximately
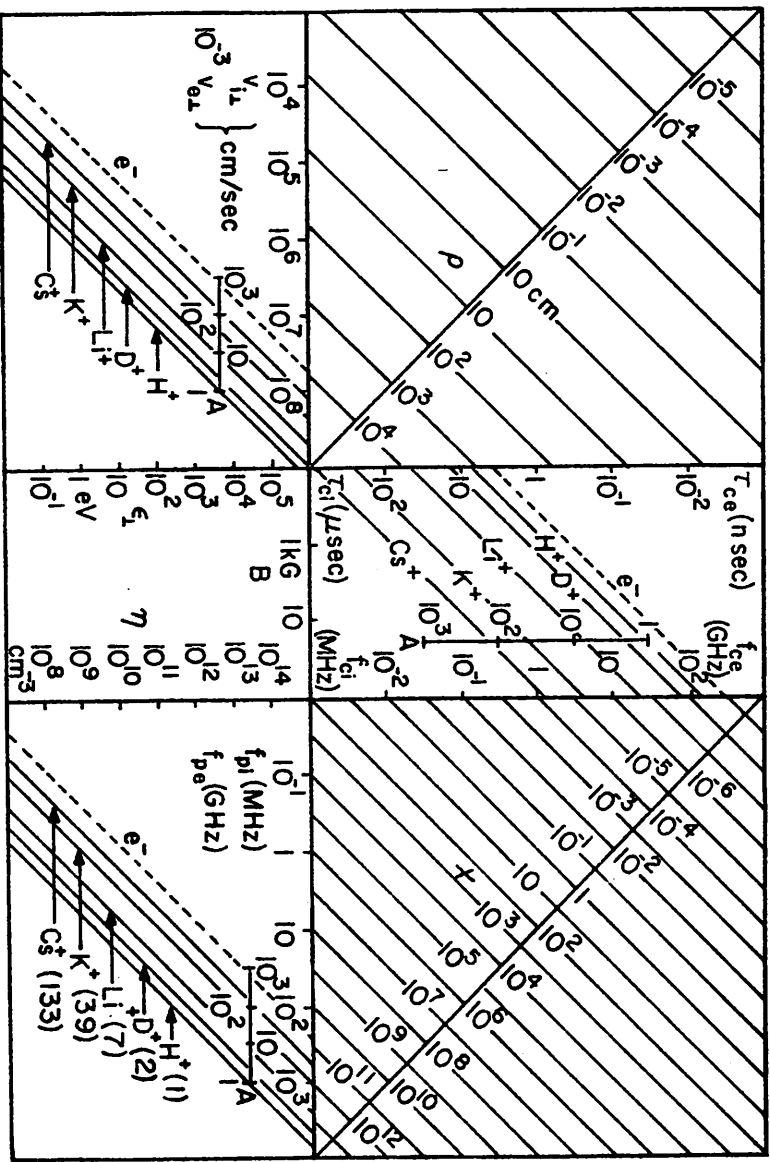
Fig. 1. A normograph for finding $V_\perp$ (particle speed), f_c (cyclotron frequency), f_p (plasma frequency), ρ (gyroradius), and χ (plasma susceptibility) from m(mass), n(number density), B(magnetic field), and $\epsilon_\perp$ (transverse energy).

$$A = \frac{e\, m_i}{q_i\, m_H}$$

$$\chi \equiv K_\perp - 1 = \frac{m_i n}{\epsilon_0 B^2} = \frac{\omega_{pi}^2}{\omega_{ci}^2} = \frac{\rho_i^2}{2 D_i^2}$$

7×10^4 cm/sec, while the gyrofrequency for K^+ ions in a 1 kG

magnetic field is found to be approximately 4×10^4 Hz in the upper

middle section of the figure. From the above two numbers, one finds

in the upper left section the corresponding gyroradius to be about

0.3 cm. Similarly, one finds the gyroradius of a 10 keV, D^+ ion in

20 kG magnetic field to be approximately 1.2 cm. This means that if

one wishes to simulate a 10 keV deuterium plasma in 20 kG magnetic

field by a 0.1 eV potassium plasma in 1 kG magnetic field, one must

scale everything down to 1/4 size. This scaling is obvious for all

lengths but the ion Debye length. The latter can be properly scaled by

making the ratio of ion Debye length to ion gyroradius identical in these

two systems. This amounts to keeping the plasma susceptibility $\mathcal{X}$

unchanged in the scaling. ($\mathcal{X} = m_i \, n \epsilon_0^{-1} \, B^{-2} = \omega_{pi}^2 \, \omega_{ci}^{-2}$). Returning to

Fig. 1, one finds that $f_{ci} \approx 1.5 \times 10^7$ Hz for the deuterium plasma in

question, and that if the density is 10^{12} cm^{-3}, then $f_{pi} \approx 1.5 \times 10^8$

(lower right section). The corresponding value of $\mathcal{X}$ is found in the

upper right section to be 10^2. One finds that in order for the potassium

plasma in question to have the same value of $\mathcal{X}$, it must have a density

of about 1.5×10^8 cm^{-3}.

For the potassium plasma used in our experiment, the typical

numbers are $T = 0.1$ eV, $n = 1.5 \times 10^9$ cm^{-3}, $B = 1$ kG and $\mathcal{X} = 10^3$.

It corresponds to a deuterium plasma with $T = 10$ keV, $n = 10^{13}$ cm^{-3},

$B = 20$ kG. It should be remembered that there are infinitely many

combinations of n, T, B values that yield the same value of $\mathcal{X}$.
Therefore, a given plasma system actually simulates an unlimited
number of different plasmas all simultaneously. It is also important
to note that all flute modes have the peculiarity of being nearly density
independent in the $\mathcal{X} \gg 1$ regime [1]. This makes all plasmas in this
regime approximately equivalent. Another remark is that the effect
of electron inertia is always negligible for flute modes $(k_{11} = 0)$. Con-
sequently, in all scaling calculations, we always consider the ion mass
and ignore any change in the electron-to-ion mass ratio. The electron-
to-ion temperature ratio, however, is not an ignorable factor. The
temperature ratio must be the same in all equivalent systems.

The scaling relations described above are based on a law of
similitude derived from the Vlasov equation, which neglects collisions.
It is rather impractical to scale various collision distances along with
other characteristic distances. Fortunately, flute modes $(k_{11} = 0)$ are
relatively insensitive to collisions, so that over a period of several
ion collision times the behavior of flutes should be essentially collision-
less. Various collision induced $k_{11} \neq 0$ modes can be differentiated by
measurements.

Collisions seriously limit the particle confinement time. It is
therefore important to know various times and distances associated
with collisions. Figure 2 is provided to facilitate finding the mean
Coulomb self-collision distance. For instance, in a 0.1 eV plasma
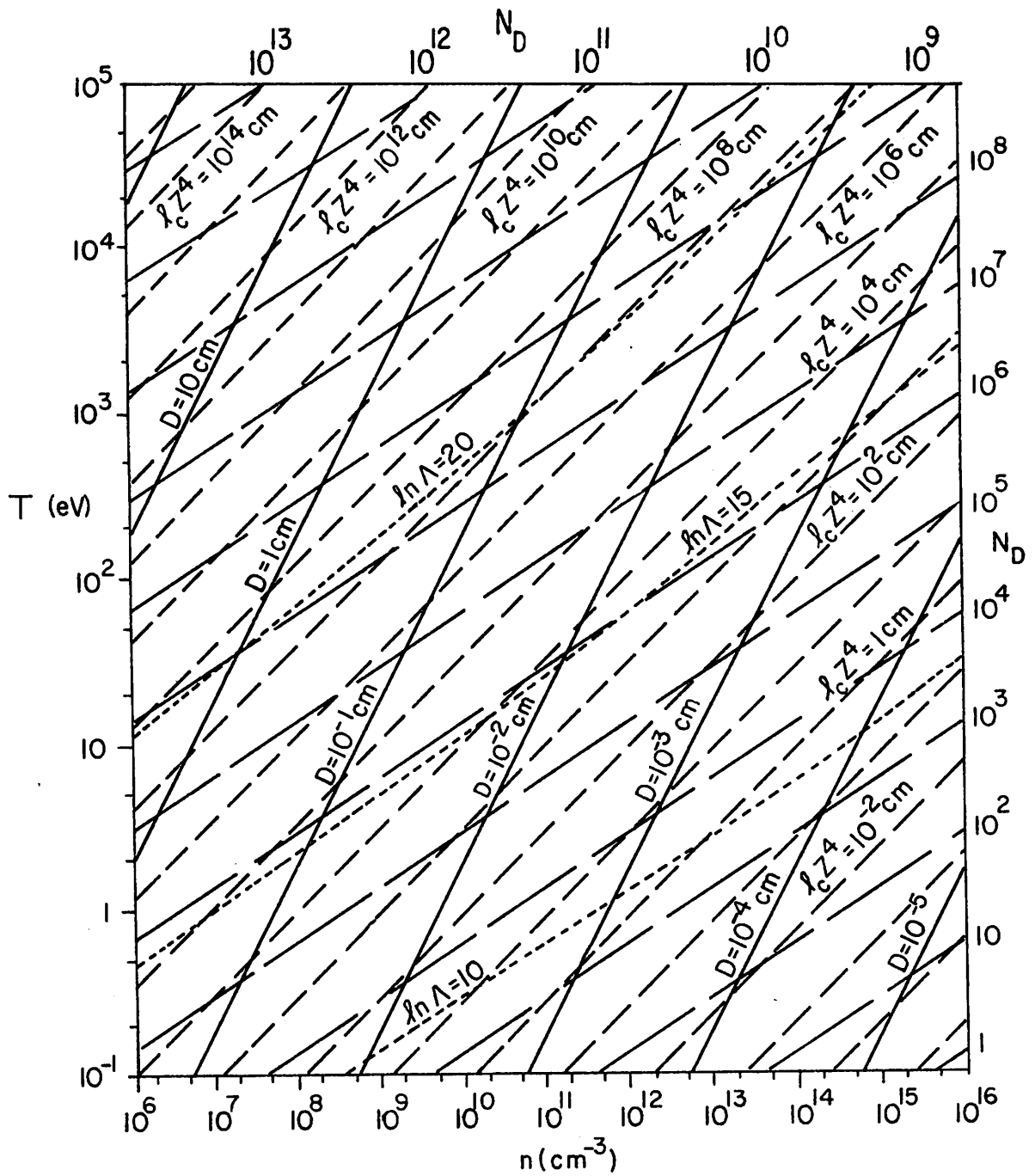
Fig. 2. A normograph for finding D (Debye length)
N_D (number of particles per Debye sphere),
ℓ_c (self collision distance) and $\ell n \, \Lambda$ from
n (number density) and T (temperature).

with a density of 1.5×10^8 cm^{-3}, the self-collision distance for both electrons and ions is slightly over 100 cm. The mean free paths for other processes can be found from Fig. 3. For instance, if the electron-neutral collision cross-section is 10^{-14} cm^2, then, for a background pressure of 3×10^{-7} torr, the electron mean free path is 10^4 cm.

Figures 1 and 2 can also be used to find other useful plasma parameters, e.g., v_e, f_{ce}, ρ_e, f_{pe}, D_e, N_D and $\ln \Lambda$.

2. APPARATUS

A cross-sectional view of the experimental device is shown schematically in Fig. 4. The main vacuum chamber has an inner diameter of 5 5/8 inches. The typical base pressure is 3×10^{-7} torr. The bottom flange of the vacuum chamber has six electrical feedthroughs for diagnostic purposes, a center port for viewing and photographing, and two oppositely located ports for mounting movable probes and a potassium oven. The oven is partially filled with high purity potassium metal and is maintained at a temperature between 200°C and 300°C, depending on the desired plasma density. Potassium molecules effuse out of the oven through a collimating nozzle and impinge on the entire ionizer-cathode located at the center of the device. The ionizer-cathode, which emits both ions and electrons, is a hot (2000°K $\pm$ 50°) tungsten mesh in the form of a roughly spherical cage 2 inches in diameter. The mesh structure is reinforced by a hollow molybdenum disc, which probably also helps form a smoother electron distribution, although its
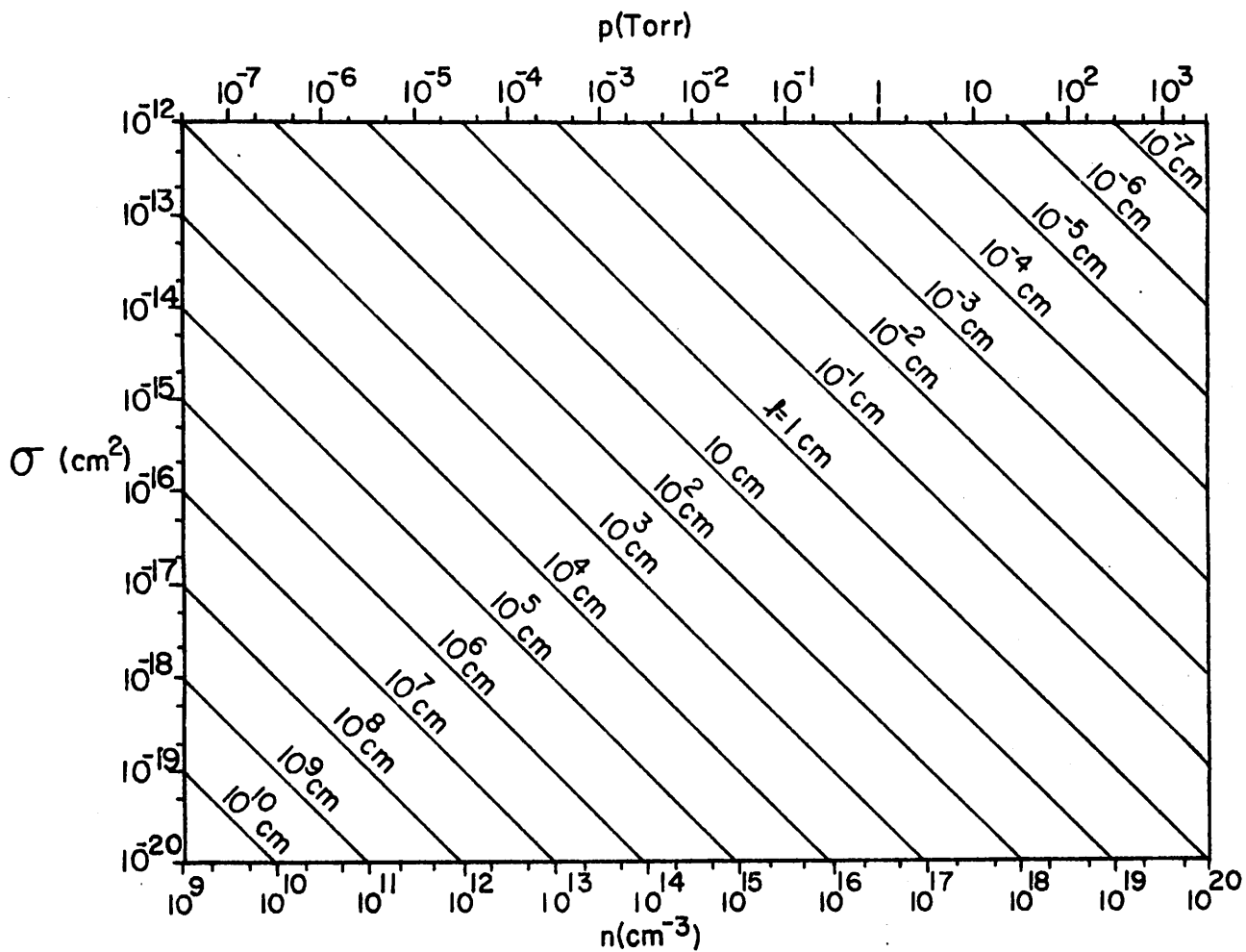
Fig. 3. A normograph for finding the mean free path from
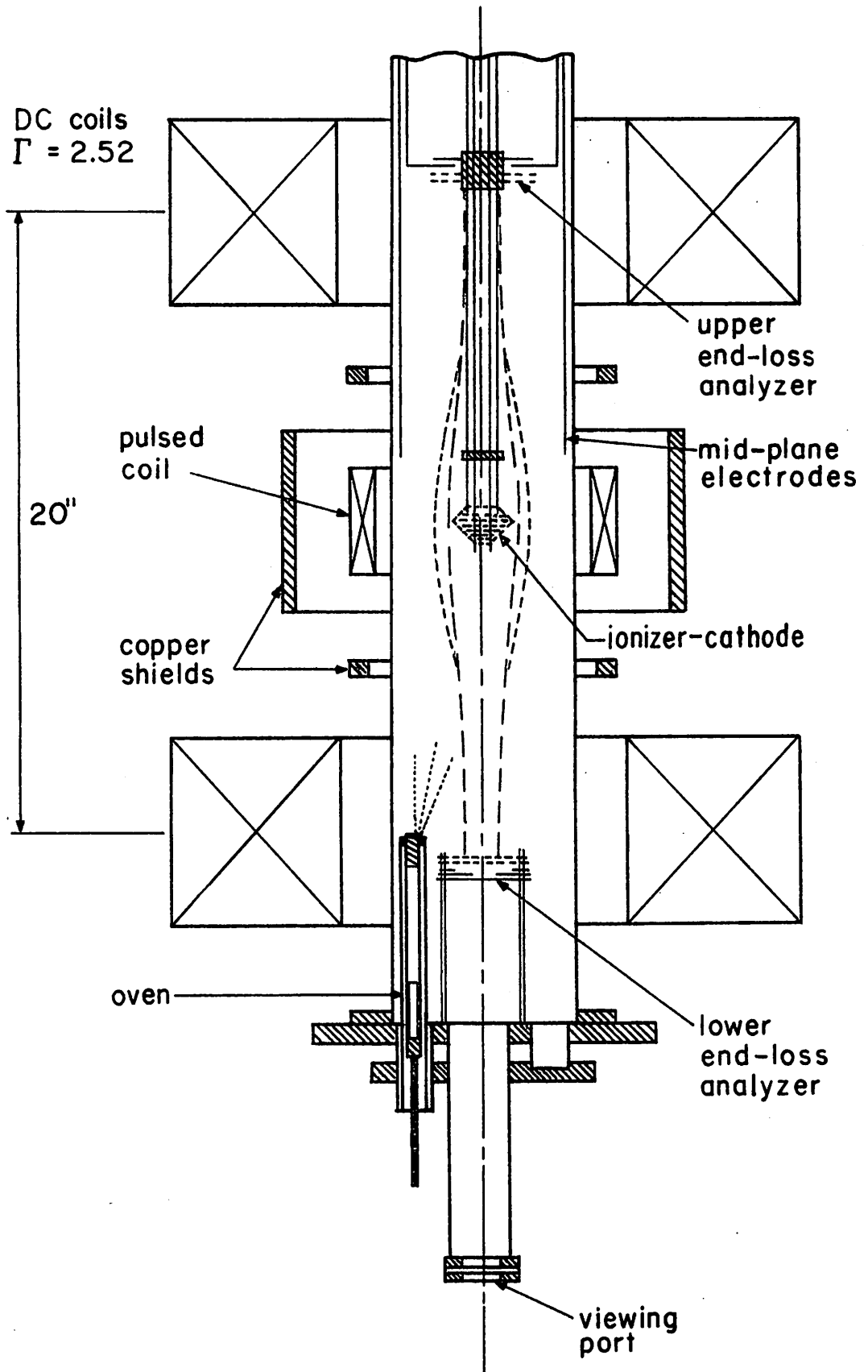σ (cross-section) and n(number density) or
p (pressure).

Fig. 4. Cross-sectional view of the experimental device.

effectiveness is uncertain. The wire separations in the mesh are small compared to the mean ion gyroradius. A set of tungsten rods suspends the ionizer-cathode from above, also providing electrical connections. These tungsten rods are arranged to form two coaxial cylindrical layers, the outer of which has a diameter of 3/4", small enough not to intercept particles emitted from near the rim of the ionizer-cathode. Prior to each data-taking shot, the ionizer-cathode is heated to a desired temperature by a 60 Hz current. Then, the current is interrupted and measurements taken before the temperature has changed appreciably.

The plasma produced by the ionizer-cathode is more or less confined in a magnetic mirror trap of mirror ratio 2.52, which is generated by two DC coils separated 20 inches center to center. Since the ionizer-cathode is a good conductor and emits electrons, it tends to inhibit flute instability in the plasma by short circuiting the electric field, $E_\perp$. In order to make this device useful for its intended purpose, we have to make the flute instability possible again by freeing at least part of the plasma from the short circuit region. This we accomplish by adiabatically decompressing the plasma with a pulsed coil. The decompression causes the plasma to expand radially (typically double the cross-section) into the region unobstructed by the ionizer-cathode. The expanded state lasts for several milliseconds, long enough for various observations. The pulsed field is confined to the center portion of the mirror trap by heavy copper shields. Consequently, a magnetic

flux surface will remain stationary near the mirror planes while expanding near the mid-plane.

The plasma is terminated outside the mirror trap by insulated end plates (gray oxidized Ta) placed typically one inch from the mirror planes. Some end-loss particles are allowed to pass through the end plates via holes and slots and are then analyzed both in time and in space by the two sets of electrodes henceforth to be referred to as the upper and lower end-loss analyzers. The electric circuit for these and other diagnostic electrodes are shown schematically in Fig. 5. Each end-loss analyzer has an ion collector placed immediately behind the insulated end plate. These ion collectors have holes and slots, matching those on the end plates but slightly oversized to make it possible for electrons to pass through without being intercepted. The holes and slots are made smaller, or narrower, than the mean ion gyroradius so that ions can be easily captured by the ion collectors. In the lower end-loss analyzer, the ion collector is split into a 1 1/4 inch central part and the remaining peripheral part. The ion current to these two parts can be monitored separately. Behind each ion collector is an electron collector, consisting basically of a large screen, a large plate, and sandwiched between them, strategically located radial strips for observing azimuthal variations and velocities of rotating perturbations in the plasma.
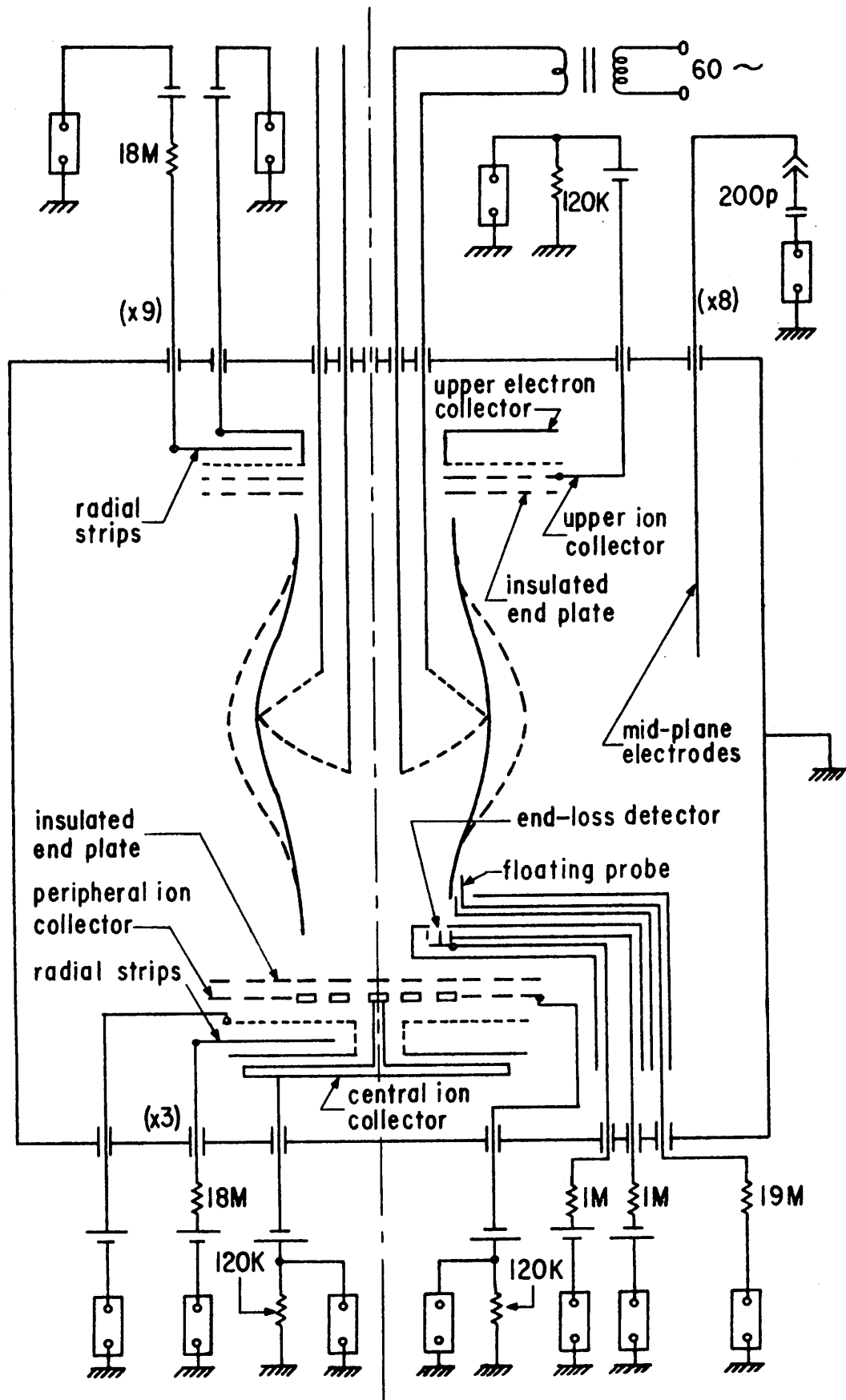
Fig. 5. Schematic diagram of diagnostic circuits. The rectangular boxes represent 1 Meg-ohm scope inputs or equivalent dummy loads. All batteries are typically 3 volts. Multiplicities of electrodes are indicated inside parentheses.

There are eight wires protruding into the mirror trap about 8 inches deep from the top and at 2 1/2 inch radius from the ionizer-cathode axis. These are used either to introduce external disturbances or to monitor signals near the mid-plane and will be referred to as the mid-plane electrodes. They are normally unbiased and are isolated from ground by at least 20 meg-ohms.

An end-loss detector and a floating probe were mounted on a sliding shaft that can be rotated about its axis located 2 1/16 inches off the vacuum axis. These are used to measure the radial distributions of the end-loss flux and the plasma potential. The end-loss detector consists of an insulated box with a 1 mm diameter sampling hole, a thumbtack shaped electron collector inside the box with the pin pointing towards the sampling hole, and a 2 mm diameter ion collector ring placed around the electron collector pin. The floating probe is an unbiased single wire probe oriented parallel to the device axis and with 20 meg-ohm total resistance to ground. The floating probe protrudes 1/2 inch into the mirror trap, while the end-loss detector stays 1/2 inch outside the mirror trap. The end-loss detector and the floating probe are separated by 3/4 inch in the plane normal to the vacuum axis.

All ion collectors in the end-loss detector and analyzers are typically biased -3 volts with respect to ground, while the electron collectors are typically biased at +3 volts above ground. The ionizer-cathode is left floating with the plasma.

3. PRELIMINARY RESULTS

The objective of this experiment is to understand the dependence of flute instability on various parameters. A comprehensive analysis of the problem has been completed and will be published elsewhere [3]. Specific calculations pertaining to the plasma in this experimental device have also been carried out [2]. Experimentally, we have observed flute oscillations of $m = 1$ to $m = 6$ modes. We were able to determine the mode number and the phase velocity quite unambiguously. However, we still do not have in our hands a reliable means of measuring the flute growth rate in a definite manner. This has so far prevented us from making meaningful comparisons between theory and experiment. Efforts are being made to improve this matter.

As a result of extensive measurements made with the movable end-loss detector and the floating probe, the zeroth order properties of the plasma are now fairly well understood. These measurements were carried out in the following manner. First, all external parameters are set to desired values and a suitable amount of 60 Hz heating current applied to the ionizer-cathode. The system soon reaches a quasi-steady state with 60 Hz fluctuations clearly present in all quantities. This condition corresponds to the first 210 ms. in Fig. 6 (time scale = 100 ms./div.). This figure shows three successive shots made with the end-loss detector and the floating probe at three different positions. The first trace in each frame shows plasma potential measured by the
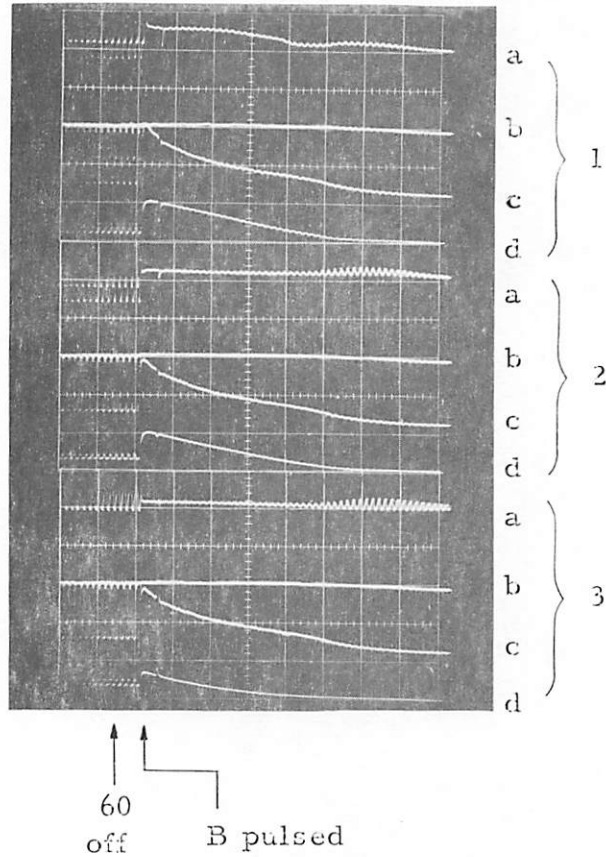
Fig. 6. Plasma potential and end-loss signals at 100 ms per major division. Three successive shots with the floating probe and the end-loss detector at three different positions. Each frame shows: a, the plasma potential (2 volts per major division); b, the total ion end-loss flux to the upper end-loss analyzer; c, the peripheral ion end-loss flux to the lower end-loss analyzer; d, the local ion end-loss flux measured by the end-loss detector (4×10^{13} ions per sec. per cm^2). The 60 Hz heating current to the ionizer-cathode is turned off at t = 210 ms. The pulsed magnetic decompression takes place at t = 256 ms.

floating probe in 2 volts per division. The second trace shows the total ion current measured by the upper end-loss analyzer. The third trace is the ion current to the peripheral part of the ion collector in the lower end-loss analyzer. The fourth trace shows the ion current measured by the movable end-loss detector. One major division here corresponds to 4×10^{13} ions per second per cm^2. At t = 210 ms. in Fig. 6, the 60 Hz heating current is suddenly cut off. All quantities quickly settle to a more or less steady value in about 20 ms., then slowly decay to zero in about 1 second due to the ionizer-cathode cooling off. Shortly after the 60 Hz current is cut off, the pulsed coil is fired (t = 256 ms. in Fig. 6), and the plasma near the mid-plane becomes temporarily decompressed. This less than 10 ms. period of magnetic decompression is the center of our interest. Figure 7 is a plot of the plasma potential and the end-loss flux as functions of radius at the mirror plane. All points on the dashed curves are obtained immediately before the decompression, while all points on solid curves are obtained at the moment of maximum decompression. All values are measured with respect to the base lines defined by the asymptotes of scope traces. The size of the mean ion gyration orbit is also shown on the figure. It is seen that the plasma extends beyond the rim of the ionizer-cathode by about two gyroradii. The end-loss distributions are strongly depressed near the axis. This is due to the fact that the central part of our ionizer-cathode is relatively cold and open. There is an inadvertent

Ion end-loss flux density

—before

—after

5 cm

r

0

ion gyro orbit size

Peripheral ion collector

Central ion collector

Peripheral ion collector
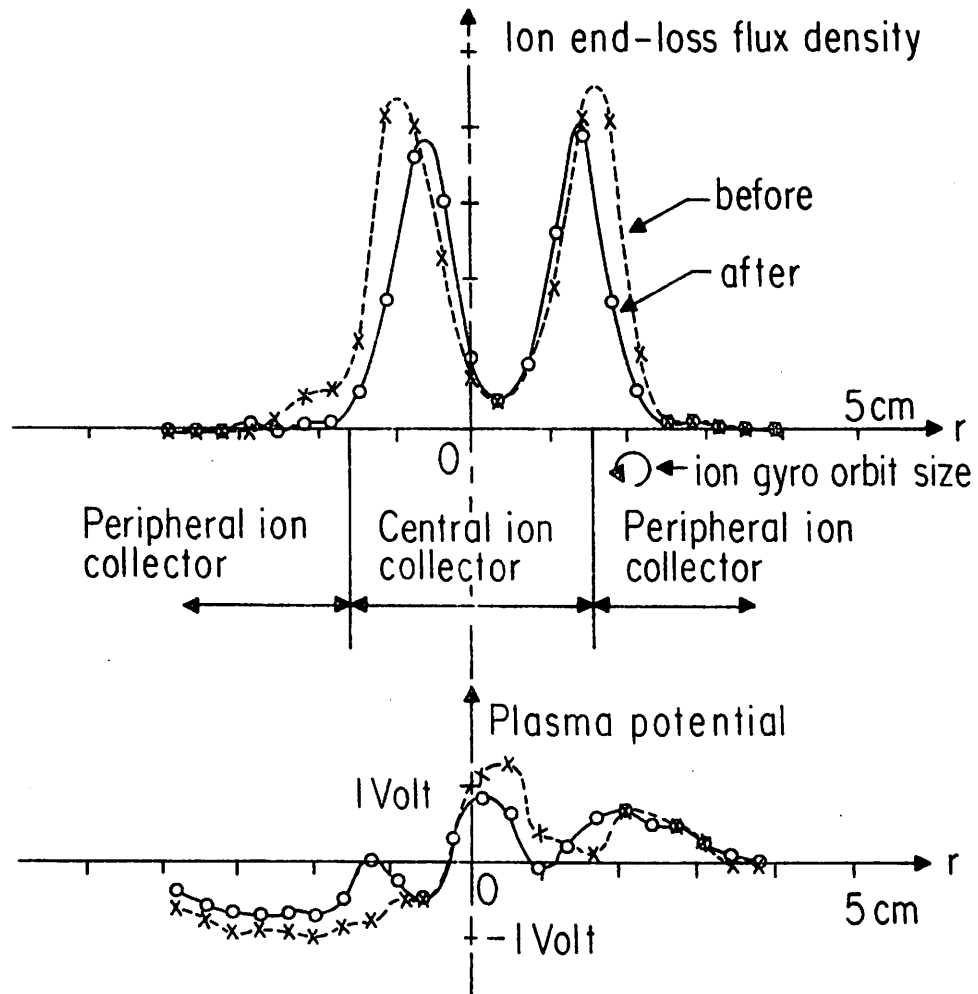
Plasma potential

I Volt

0

r

5 cm

— I Volt

Fig. 7. Distributions of the ion end-loss flux density and the plasma potential measured at the lower mirror plane. Dashed curves are obtained before the magnetic decompression. Solid curves are obtained at the moment of maximum decompression. External parameters: oven temperature = 240° C, mirror plane magnetic field = 2.0 kG.

misalignment of the ionizer-cathode from the vacuum axis. This also means misalignment from the magnetic axis, and is probably responsible for the small bump on the left-hand skirt of each end-loss distribution curve.

In Fig. 7, the end-loss distribution appears to be compressed by the magnetic decompression. This apparent contradiction is due to the fact that the decompression is confined to the region near the mid-plane. As the decompression goes on, fewer and fewer magnetic flux surfaces become intercepted by the ionizer-cathode at the mid-plane. At the mirror planes, since these flux surfaces remain stationary, we see the opposite phenomenon of a shrinking image of the ionizer-cathode that is intercepting less and less magnetic flux. The decompression increases the mirror ratio (from 2.52 to 5.04); i.e., it reduces the size of the loss-cone in the velocity space. If one assumes that the particles are scattered in and out of the loss-cone faster than they can be transported out of the mirror trap so that the velocity distribution remains nearly isotropic at all times, then one would expect a smaller end-loss flux as the loss-cone is made smaller by the decompression. Figure 7 shows that this is the case.

Assuming the continuity of particle flux over the entire length of every magnetic flux tube, one can infer the distribution of end-loss flux at the mid-plane from the curves in Fig. 7. This is done simply by expanding the curves horizontally about the magnetic axis by the

square-root of the mirror ratio (Γ = 2.52 for the dashed curve, 5.04

for the solid curve). The result is shown in Fig. 8, where the relative

amplitudes have been renormalized to equalize the peaks. The effec-

tiveness of the magnetic decompression is indicated by the expansion

of the skirts of end-loss flux curves. The positions of peaks, however,

do not change as much, because the ionizer-cathode continues to emit

particles during the decompression period. Similar expansion of the

potential curves are also given in the same figure.

Figures 7 and 8 were obtained with the oven temperature at

240°C and the mirror-plane magnetic field at 2.0 kG. Measurements

were repeated with various other combinations of parameters. Figures

9 and 10 summarize the results of these measurements, showing only

the expanded state (solid curves in Figs. 7 and 8). The end-loss curves

are quite reproducible and are believed to be reliable. The plasma

density at the mid-plane can be estimated from these curves. The

vertical scale in Fig. 7 is approximately 8×10^{12} ions per second per

square centimeter per division. By continuity, the same end-loss flux

per flux tube exists at the mid-plane. But since the flux tubes have a

larger cross-section at the mid-plane, the vertical scale must be

divided by the mirror ratio. For the solid curve, this results in

1.6×10^{12} ions per second per square centimeter per division. Now,

at the mid-plane, the mean velocity of the loss-cone ions is approxi-

mately equal to the mean ion thermal velocity, about 10^5 cm/sec.
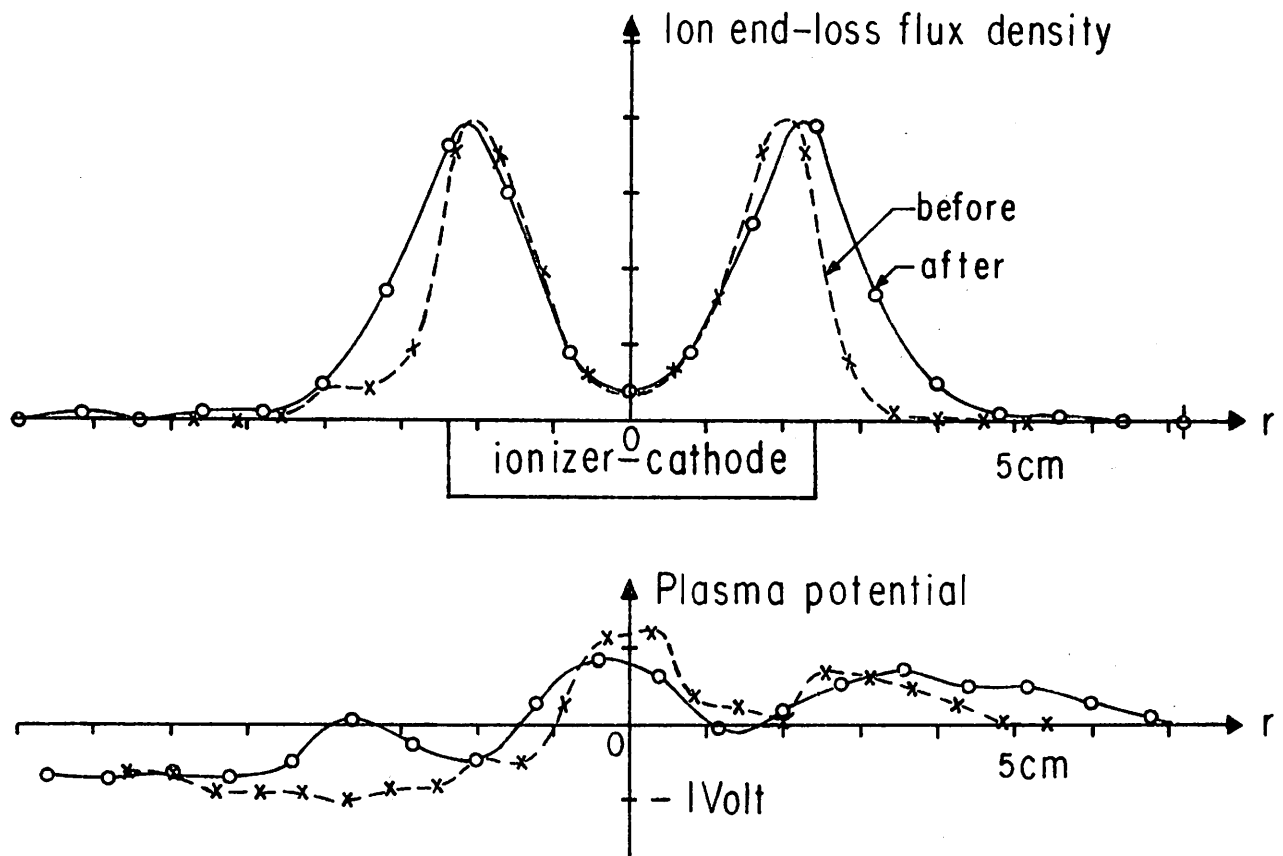
Fig. 8. Curves in Fig. 7 translated to the mid-plane, showing the expansion of plasma produced by the magnetic decompression. The end-loss curves have been renormalized to equalize the peaks.

Hence, a division on the vertical scale is also equivalent to a loss-cone ion density of 1.6×10^7 cm^{-3} at the mid-plane. Assuming an isotropic velocity distribution, the ratio of the loss-cone ion density to the total ion density is equal to the fractional volume of a loss-cone in the velocity space, given by $0.5 - 0.5 (1 - \Gamma^{-1})^{\frac{1}{2}}$, where Γ is the mirror ratio [2]. For $\Gamma = 5.04$, the above ratio is equal to 0.053, which makes one division on the vertical scale equal to a total ion density of 3×10^8 cm^{-3} at the mid-plane. Thus the peak plasma density in Figs. 7, 8 and 9 is about 1.2×10^9 cm^{-3}, while in Fig. 10 it is about 2×10^9 cm^{-3}. (The plasma density in Fig. 10c is lower because the magnetic decompression is applied at a time later than in others.) The less than a factor of two increase in the plasma density is lower than the expected factor of three increase of potassium vapor pressure due to a 30° increase in the oven temperature. The discrepancy is probably due to a greater beam divergence at the higher density.

The measured distribution of the plasma potential is less reproducible, and seems to be considerably distorted by the presence of the movable end-loss detector and the floating probe. Potential differences well in excess of kT/e were measured. The distribution of electric field would produce a non-rigid-body rotation of the plasma at speeds comparable to those of flute modes. All these irregularities must be reduced before any meaningful comparison with theoretical calculations can be made. The first obvious step is to understand and reduce the probe perturbation.
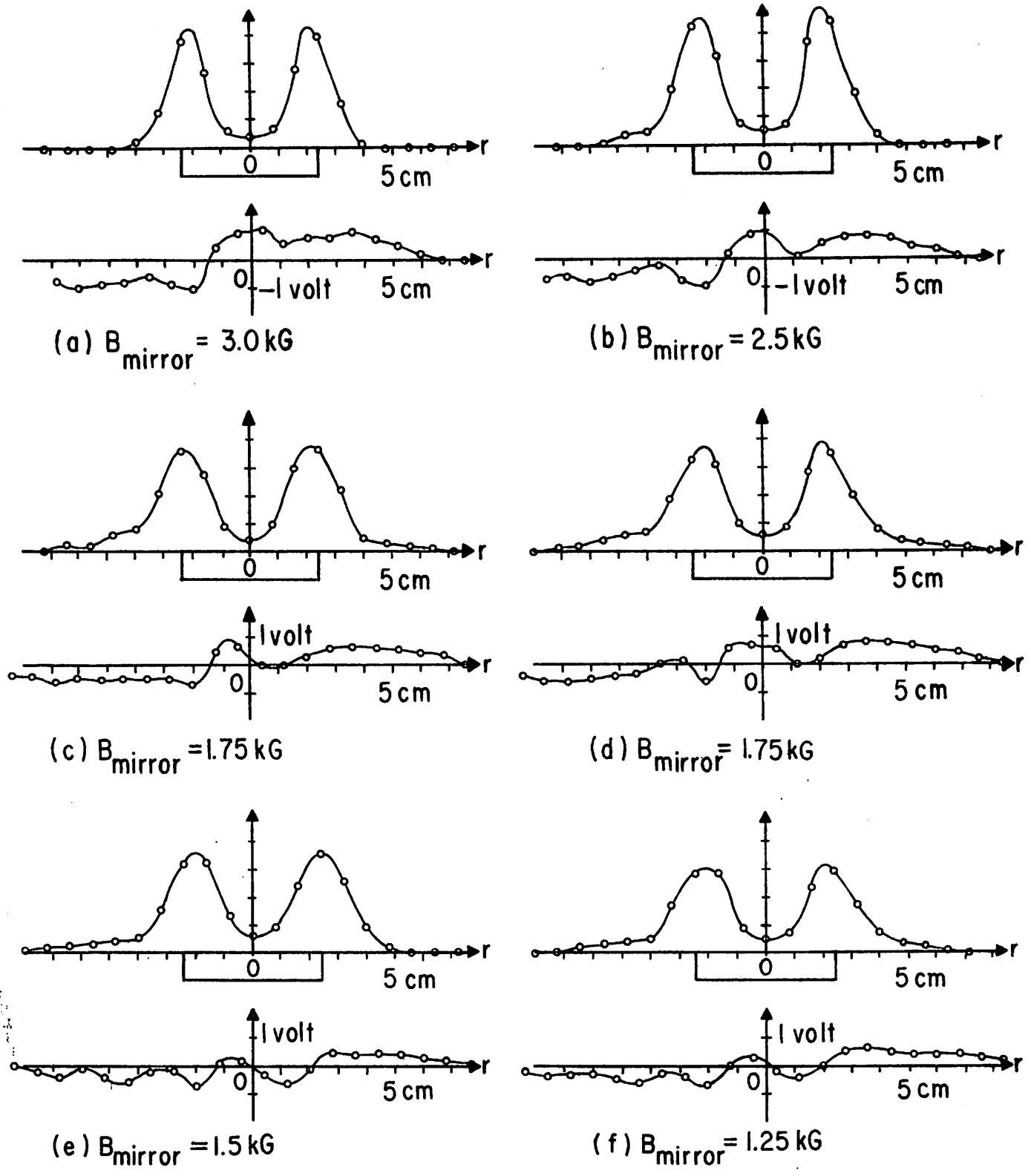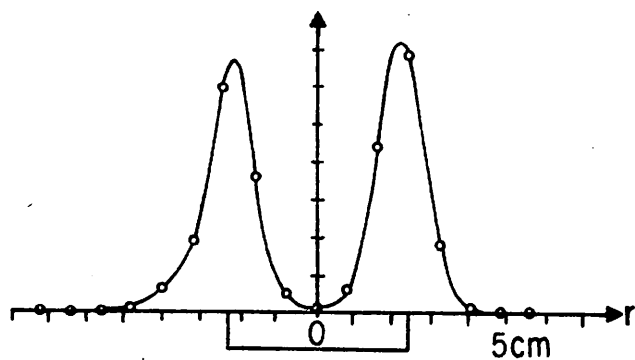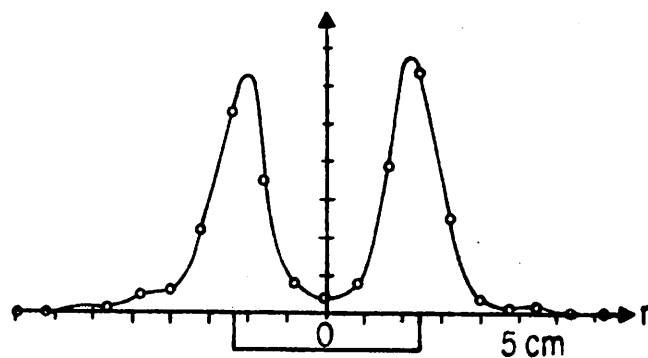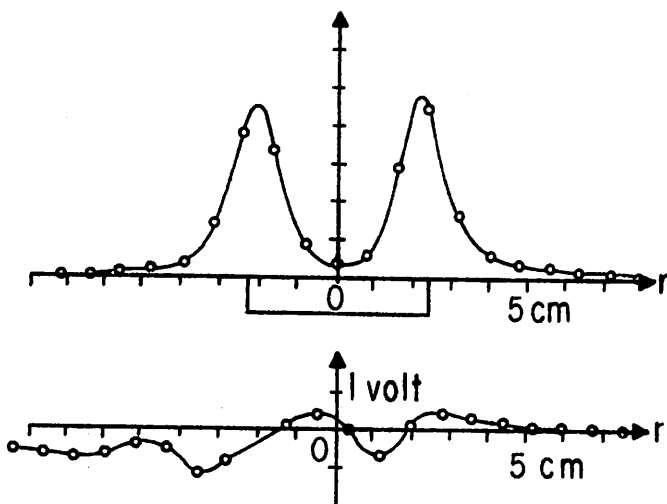
Fig. 9. End-loss and potential distribution curves corresponding to the solid curves in Fig. 8. measured at different values of the magnetic field, with an oven temperature of 240° C.

(a) $B_{mirror} = 3.0\,kG$

(b) $B_{mirror} = 2.5\,kG$

(c) $B_{mirror} = 2.0\,kG$

(d) $B_{mirror} = 1.75\,kG$

Fig. 10. End-loss and potential distribution curves
corresponding to the solid curves in Fig. 8
measured at different values of the mag-
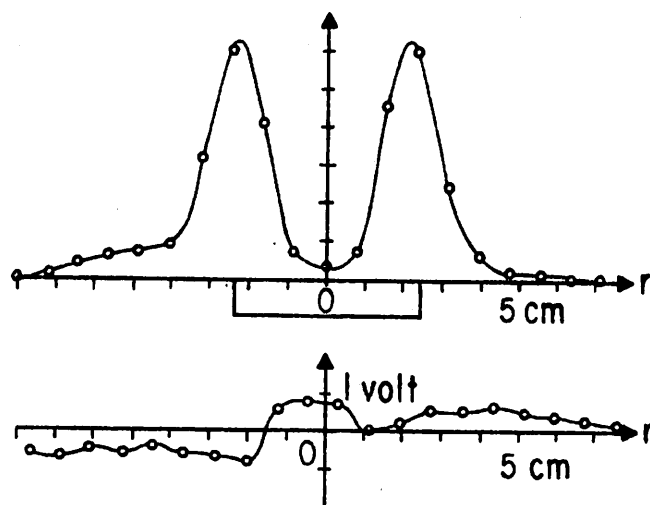netic field, with an oven temperature of 270° C.

Figure 11 gives an example of perturbations produced by the movable detector and probe. These are again three successive shots taken with the end-loss detector and the floating probe at three different positions. The upper photograph is essentially the same as Fig. 6. The lower photograph shows signals detected during the decompression period by the mid-plane electrode at $\theta = -15^{o}$, the radial strips at $\theta = -15^{o}$, and $\theta = 0^{o}$ in the upper end-loss analyzer, and the radial strip at $\theta = 0^{o}$ in the lower end-loss analyzer. The time scale for the lower photograph is 2 ms. per major division, and the pulsed coil is fired at t = 1.6 ms. In the first shot, no regular oscillation of the plasma is observed. In the second shot, a regular oscillation is triggered by the decompression pulse. In the third shot, a regular oscillation is present even before the decompression. (The absence of signals between t = 1.6 ms. and t = 4.0 ms. is probably due to a temporary suppression of the end-loss flux by the suddenly increased mirror ratio). These oscillations can be seen as hash in the third traces of second and third shots of the upper photograph. This type of oscillation has been observed with the end-loss detector located on either side of the plasma axis, wherever the end-loss flux is appreciable. The floating probe, which was mounted on the same rotating shaft as the end-loss detector, was always on one side of the plasma axis when these oscillations were observed. This leads us to believe that the larger end-loss detector is the main source of potential perturbations in these measurements.
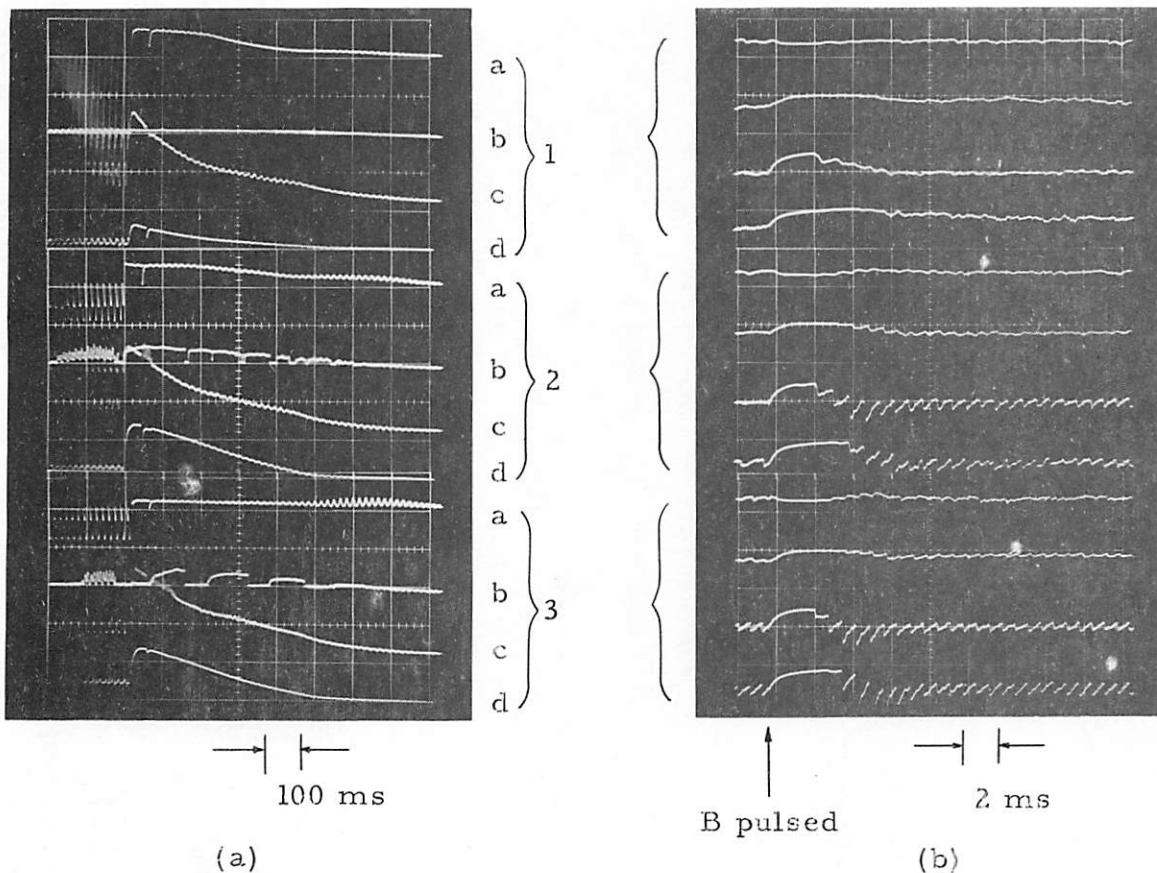
Fig. 11. Flute oscillations induced by the detector and probe perturbation. (a). Plasma potential and end-loss signals at 100 ms per major division. Three successive shots similar to those in Fig. 6(b). Oscillation signals during the decompression period of each of the three shots at 2 ms per major division. Each frame shows: (a), the signal picked up by an unbiased mid-plane electrode at $\theta = -15^{\circ}$; (b), the electron current to a radial strip, biased + 3 volts, at $\theta = -15^{\circ}$ in the upper end-loss analyzer; (c), the electron current to a radial strip, biased + 3 volts, at $\theta = 0^{\circ}$ in the upper end-loss analyzer; (d), the electron current to a radial strip, biased + 3 volts, at $\theta = 0^{\circ}$ in the lower end-loss analyzer.

Further measurements of the plasma potential should therefore be made with a smaller floating probe in the absence of the end-loss detector.

An analysis of phase shifts among different traces in Fig. 11 reveals the fundamental oscillation at 1.5 kHz to be a high mode number perturbation rotating in the negative θ direction (the direction of ion gyration). Figure 12 shows similar oscillations with the same external parameters as in Fig. 11, but with the end-loss detector moved to a different position. Here we have more traces available for mode analysis. The phase of oscillation shifts in the negative θ direction and passes through six oscillation cycles as we go over 360 degrees in θ, indicating an $m = 6$ perturbation rotating in the negative θ direction. The oscillation frequency is 750 Hz before and after decompression and slows down to 500 Hz during the decompression period. This is in qualitative agreement with our theoretical prediction [2]. The phase relations also indicate the perturbations to be exactly parallel to the plasma axis, which is characteristic of flute modes.

Some oscillations that appear exclusively during the decompression period were observed when both the end-loss detector and the floating probe were moved out to at least two ionizer-cathode radii from the plasma axis, i.e., when the perturbations were substantially reduced. Figure 13 suggests a growing oscillation, while Fig. 14 is probably indicative of either a low m-number flute instability or a velocity space instability that drives particles out of the mirror trap.
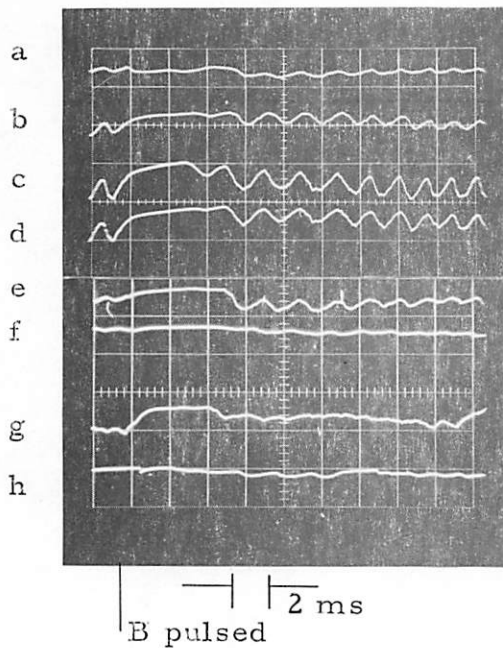
Fig. 12. Detector and probe induced oscillation and the effect of decompression. (2 ms per major division). The magnetic unbiased decompression starts at t = 1.8 ms. Trace (a), signal picked up by an unbiased mid-plane electrode located at $\theta = -15°$. Traces (b), (c), (d), (e), (f) and (g) electron currents to radial strips, all biased + 3 volts, located at $\theta = -15°$, $0°$, $45°$, $135°$, $225°$, and $270°$ in the upper end-loss analyzer. Trace (h), electron current to a radial strip, biased + 3 volts, located at $\theta = 0°$ in the lower end-loss analyzer. Phase relations among the traces show the oscillation to be an m = 6 flute rotating in the negative θ direction. This type of oscillation is highly reproducible.
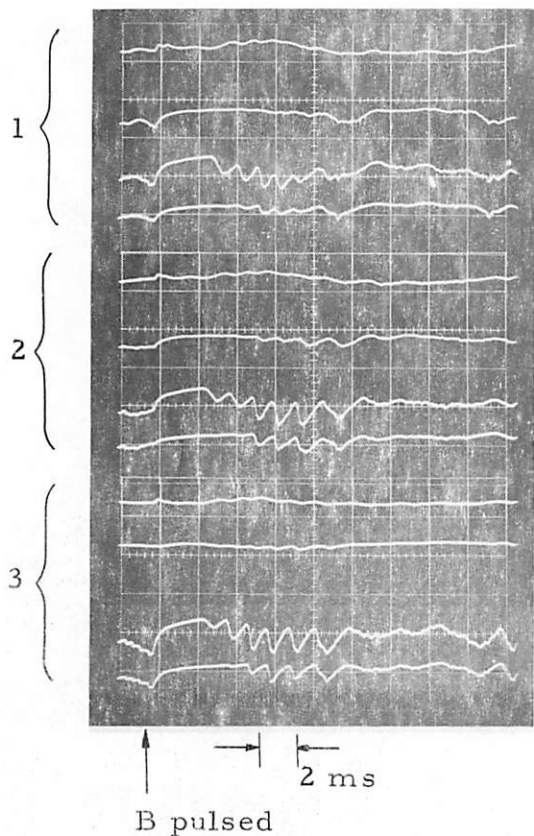

Fig. 13. Oscillations appearing only during the decompression period. (2 ms per major division). These are three successive shots under the same conditions, showing the same set of signals as in Fig. 11(b). Reproducibility is demonstrated. This type of oscillation occurs only under reduced detector and probe perturbations.
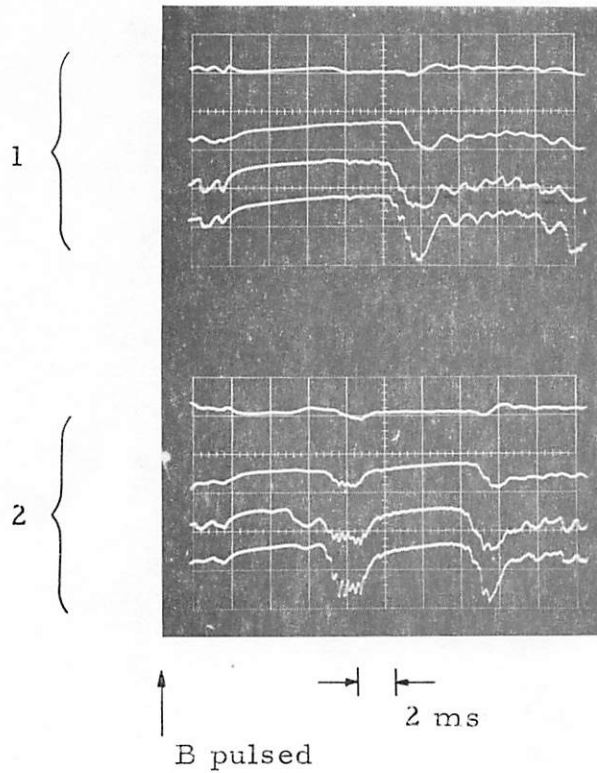
Fig. 14. Instability signals during the decompression period.
(2 ms per major division). These are two successive shots under
the same conditions, showing the same set of signals as in Fig. 11(b).
This type of signal also appears only under reduced detector and
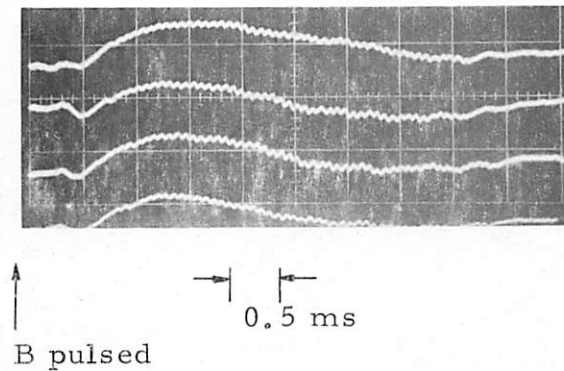probe perturbations, and is qualitatively reproducible.

Fig. 15. Flute oscillation in the decompressed plasma observed
before the introduction of the movable end-loss detector and the
floating probe. (0.5 ms per major division). Electron currents
at $\theta = 45°$, $90°$, $180°$, and $225°$ are shown. The magnetic decom-
pression starts at $t = 0.27$ ms.

Before the movable detector and probe were incorporated into the device, we observed flute type oscillations of m = 1, 2, 3, 4, and 6 modes, all rotating in the negative θ direction [2]. An example is shown in Fig. 15. The time scale is 0.5 ms. per major division. The oscillation at 13.3 kHz is an m = 4 mode, and is definitely not induced by a perturbing probe or detector. Unfortunately, we cannot give a definite interpretation of these data, because we have only rather uncertain information about the distribution of plasma density and virtually no information about the distribution of electric field.

Oscillation signals detected at various locations are very useful for determining mode patterns and phase velocities, but they do not tell whether an oscillation is stable or unstable, i. e., whether the oscillation causes an outward transport of particles across magnetic flux surfaces. An attempt was made to measure the net radial plasma transport with a specially shaped upper end-loss analyzer [2]. The results were inconclusive mainly due to large fluctuations in the ion end-loss flux to the upper end of the device.

Indications of anomalous plasma transport are sometimes present in the end-loss current to the peripheral ion collector of the lower end-loss analyzer. The third traces in Figs. 16a, b, and c correspond to this current. (These photographs are similar to the ones in Fig. 6 except for the 2 ms. per division time scale.) When the plasma is very quiet, the peripheral ion current behaves as the third trace of Fig. 16a
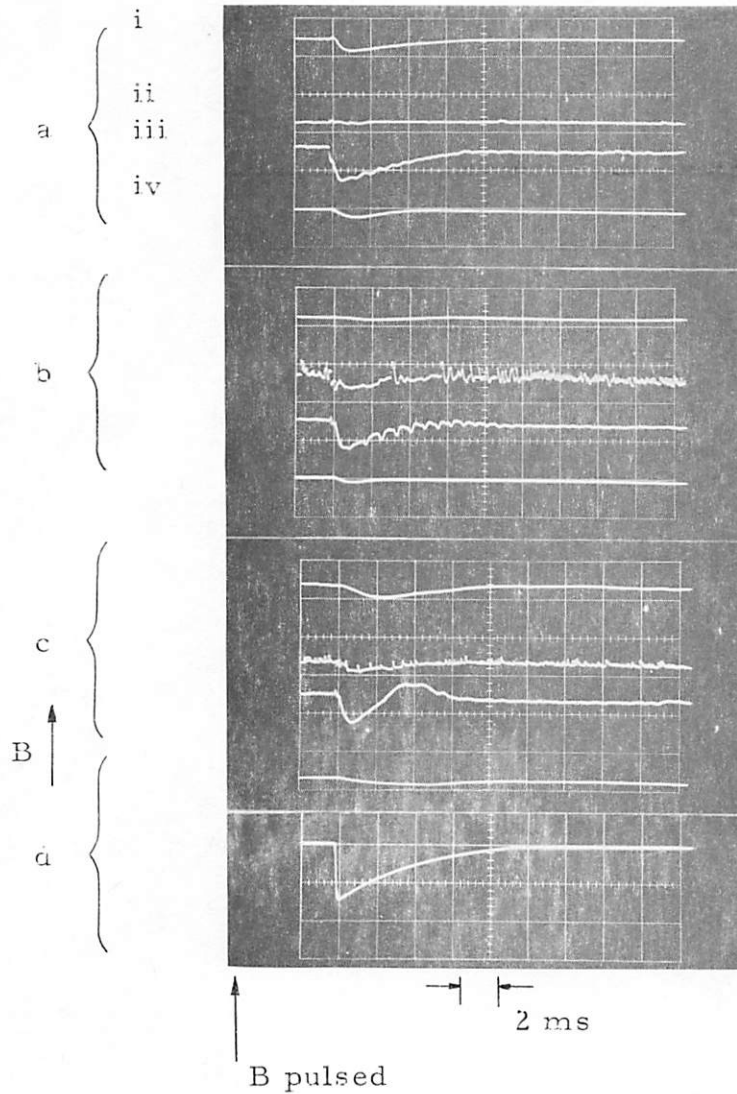
Fig. 16. (a, b, c). Three shots with the end-loss detector
and the floating probe at three different positions, showing
successively a quiet condition, an oscillatory condition,
and an unstable condition. (2 ms per major division.)
Except for a different time scale, each frame shows the
same set of signals as in Fig. 6: namely, (i) the plasma
potential, (ii) the total ion end-loss flux to the upper end-loss
analyzer, (iii) the peripheral ion end-loss flux to the lower
end-loss analyzer, (iv) the local ion end-loss flux measured
by the end-loss detector. The magnetic decompression
starts at t = 1.8 ms. The temporal variation of the mag-
netic flux density at the mid-plane is shown in Fig. 16(d).

during the decompression period. In Fig. 16b, the perturbation due to the movable end-loss detector is increased and an oscillation is excited by the decompression pulse. The periodic dips in the peripheral ion current are presumably indicative of a rotating flute passing over the end-loss detector. (The end-loss detector casts a strip shadow on the peripheral ion collector.) In Fig. 16c, the peripheral ion current recovers from the depressed value at an anomalously fast rate and even overshoots the normal level of the current. It seems that the magnetic decompression has caused a low m-number flute instability which rapidly transports some plasma into the peripheral region and produces a large end-loss signal to the peripheral ion collector.

Much more definite measurements of flute growth are necessary for drawing useful conclusions from the experiment. Two new schemes are presently under active development. One scheme involves further segmentation of the ion and electron collectors in the lower end-loss signal. The other scheme involves the use of a pulsed plasma camera. This should provide very fine spatial resolution, but the time resolution would necessarily be coarse.

We now go into the discussion of some miscellaneous points in the experiment. Figure 16d shows the variation of the magnetic field at the mid-plane during the decompression period. The pulsed current from the capacitor reduces the magnetic flux density to half the DC value in about 0.25 ms. The capacitor is then crowbarred and the

magnetic field recovers to the DC state with an e-folding time of approximately 5 ms. Since the ion cyclotron period at 0.8 kG is about 30 μs. (cf. Fig. 1), the 50% change of magnetic flux density in 250μs. is a fairly adiabatic process. The L/R time of the vacuum wall is about 100μs. and that of the ionizer-cathode is much shorter. The magnetic surfaces and the plasma contained therein should therefore be able to expand freely without being frozen-in by the ionizer-cathode. This has already been shown to be true in Figs. 7 and 8. It is interesting to note that though the ionizer-cathode is not conductive enough to freeze-in the magnetic lines of force, it is conductive enough to stabilize unstable flute modes within its boundary. The difference lies in the current loop involved in each case. For the case of the pulsed magnetic field, the induced current completes its loop inside the ionizer cathode. While for the case of flute stabilization, the ionizer-cathode only serves to short circuit one end of a pair of oppositely charged plasma tubes. If the other end is terminated in a cold or insulated surface, then the time constant of the current loop is determined mainly by the inductance and capacitance of the pair and the conductivity of the plasma along and across the magnetic lines of force. The dominant factors are usually the inductance of the loop and the cross field resistance of the plasma. A rough estimate shows the associated L/R time constant to be much shorter than an ion cyclotron period.

In Fig. 16, the peripheral ion current seems to take about 0.5 ms. longer to change than the pulsed magnetic field. The time lag can be

approximately accounted for by the ion time of flight between the mid-plane and the mirror plane. The peripheral ion current is depressed during the decompression period, because both the shape and the amplitude of the end-loss distribution are changed by the decompression (cf. Fig. 7), resulting in a smaller integrated end-loss flux in the peripheral region. The radial compression of the distribution curve was explained in conjunction with Fig. 6 as a geometrical effect. The reduced magnitude of the end-loss flux was attributed to the reduced loss-cone volume in the velocity space, on the assumption that the velocity distribution remain nearly isotropic at all times. A look at Fig. 2 shows the Coulomb self collision distance in our device to be somewhat less than the mirror-to-mirror distance. This justifies our previous argument that the velocity distribution remains nearly isotropic because the ions can be scattered in and out of the loss-cone faster than they can escape from the mirror trap. At larger radii, where the plasma density is an order of magnitude lower, the ion self collision time is an order of magnitude longer (≈ 5 msec), and the assumption of velocity isotropy can no longer hold. In this region, we expect the end-loss flux to be suppressed by the sudden increase of the mirror ratio for a longer period. This conjecture seems to be consistent with the fourth trace of Fig. 16c. (Notice that, since it is taken at a larger radius, the current level is lower than in 16a and 16b.)

In summary, we have succeeded in producing and decompressing a potassium plasma in our experimental device with good reproducibility. The experimental data on end-loss distribution can be interpreted quite thoroughly. Our measurement of the electric field, however, seems to be seriously distorted by perturbing objects and needs to be improved. Various flute oscillations have been observed. We were able to determine their mode numbers and phase velocities quite unambiguously. However, we need more reliable methods to determine the flute growth (or transport) rate.

The device should also be useful for various other experiments, e.g., variation of the configuration, universal instabilities, resonant heating and plasma turbulence.

ACKNOWLEDGMENTS

REFERENCES

[1]   C. K. Birdsall, J. A. Byers, and T. Y. Chang, Low Temperature Plasma Experiment for Study of High Temperature Plasma Instabilities, Electronics Research Laboratory, Technical Memorandum M-72, University of California, Berkeley (1964).

[2]   T. Y. Chang, Flute Oscillations in Mirror Confined Plasmas: Theory and Experiment, Dissertation, University of California, Berkeley, (1966).

[3]   T. Y. Chang, Flute Oscillations in Bounded Plasmas and the Effect of Incoherently Precessing Ions, Plasma Physics, 9, No. 3, pp. 275-300, May/June 1967.